Two-dimensional electron gas at the (001) surface of ferromagnetic EuTiO₃

R. Di Capua,[1,2,*] M. Verma,[3] M. Radovic,[4] N. Plumb,[4] J.H. Dil,[4,5] Z. Ristic,[6] E.B. Guedes,[4,5] G.M. De Luca,[1,2] D. Preziosi,[7] Z. Wang,[4] A. Weber,[4,5] R. Pentcheva,[3] and M. Salluzzo[2,**]

[1] *Dipartimento di Fisica, Università di Napoli "Federico II", Complesso Monte Sant'Angelo via Cinthia, 80126 Napoli, Italy*
[2] *CNR-SPIN, Complesso Monte Sant'Angelo via Cinthia, 80126 Napoli, Italy*
[3] *Department of Physics and Center for Nanointegration (CENIDE), Universität Duisburg-Essen, Lotharstr. 1, 47057 Duisburg, Germany*
[4] *Photon Science Division, Paul Scherrer Institut, 5232 Villigen PSI, Switzerland*
[5] *Institute of Physics, École Polytechnique Fédérale de Lausanne, 1015 Lausanne, Switzerland*
[6] *Vinča Institute of Nuclear Sciences, Belgrade Serbia*
[7] *Université de Strasbourg, CNRS, IPCMS UMR 7504, 67034 Strasbourg, France*

S1 - Deposition and structural characterization of EuTiO₃ (ETO) films

EuTiO₃ films were *in-situ* grown by Pulsed Laser Deposition (PLD) in 10^{-6} mbar molecular oxygen partial pressure (base pressure 1×10^{-9} mbar) at 720°C on 5x10x0.5 mm³ TiO₂-terminated (001) SrTiO₃ (STO) single crystals using the facility available at the Surface/Interface Spectroscopy (SIS, X09LA) beamline of the Swiss Light Source (SLS) - Paul Scherrer Institute. The number of unit cells (uc) (from 2 to 15 uc) and the structural quality of the samples was monitored during the growth by *in-situ* reflection high-energy electron diffraction (RHEED) and after deposition using LEED (Low Energy Electron Diffraction). We have also deposited a 15uc EuTiO₃ sample on a SrRuO₃ buffer layer to improve contact to the ground. In Fig. S1a we report the RHEED intensity vs. time of the specular and first order diffraction spots during the growth of a nominal 15uc EuTiO₃ (ETO) film, and in Fig. S1b the final RHEED pattern. Regular oscillations are visible during the growth, while the final RHEED pattern show the high structural quality of the surface.

As grown samples are insulating, and are charging under the beam irradiation, thus they cannot be measured by ARPES unless after an unusual long exposure to the intense synchrotron radiation beam (up to 24 h). In order to get a conducting surface, each sample was annealed in Ultra High Vacuum (UHV) at 600 °C for one hour. This results in a metallic surface state, which was studied by ARPES. After this procedure, the ETO surface state is directly measured without the need of a further long irradiation, and remains stable at low temperature, for up to 24h. After that, we do see a degradation indicating that the surface is contaminated. An annealing performed with the same procedure described above restores the surface state. The annealing process does not affect the 1x1 surface structure and the in-plane lattice parameters, as demonstrated by the combination of RHEED and LEED measurement shown in Fig. S1b and Fig. S1c respectively. From RHEED (Fig. S1b) and LEED (Fig.S1c) data, we can accurately measure the in-plane lattice parameters as function of the ETO thickness, which are found to be identical to that one of the STO substrate, thus perfectly matched with the STO in-plane lattice.

In order to further characterize the samples structural properties, we performed ex-situ x-ray diffraction measurements using a lab-based diffractometer at the University of Strasbourg (Rigaku Smartlab (9 kW) diffractometer in parallel beam geometry equipped with a Cu kα1 source (kα1 = 1.5406 A˚) and a Ge(220) monochromator). The perfect in-plane matching between the ETO overlayer and the STO substrate is confirmed by reciprocal space mapping x-ray diffraction data around the (103) diffraction peak, as shown in Fig.S1d for the ARPES measured 15 uc ETO sample. From these data we can also see that the (103) diffraction peak of STO and ETO cannot be separated, suggesting a similar c-axis.

In Fig. S1e, we show θ−2θ x-ray diffraction on the same sample. In Fig. S1f we also show data for thinner ETO films, i.e. an 8uc ETO protected by a LAO epitaxial overlayer, grown in the same deposition conditions. The LAO capping preserves the valence of Eu, which on the other hand changes at the surface from Eu²⁺ to Eu³⁺ if exposed to moderate oxygen pressure or to ambient atmosphere.

Both samples show Pendellösung size effect fringes at the left and at the right of the STO (00L) peaks, which are related to the finite thickness of overlayer. The main ETO (00L) peaks are not separated at these low thicknesses from the STO Bragg peaks, however we can get quite precise information about the ETO c-axis from a fitting of the (001) data using dynamical x-ray diffraction code as implemented in the software Gen-X, widely used to analyze data for thin epitaxial films and multilayers [S1]. We modeled the systems as the combination of the STO bulk (TiO₂ terminated), and nominal ETO (and LAO for the heterostructure) layer thicknesses, as inferred from the RHEED oscillations during the growth. The obtained fits are very accurate (R-factor<=.2) and are very sensitive to the c-axis of the ETO (and LAO) layer, as the periodicity of the Pendellösung fringes depends on them). For the non-capped ETO film we find a c-axis of 3.92± 0.01 Å, and for the capped film a c-axis of 3.91± 0.02 Å for ETO and of 3.790± 0.005 Å for LAO (the error in the estimation of the c-axis for the heterostructure is larger and is determined from the sensitivity of the fit to this parameter). A slight elongated c-axis in the non-protected ETO film suggests a higher oxygen vacancy concentration, due to the change in the oxidation of Eu under air exposure.

Corresponding Authors
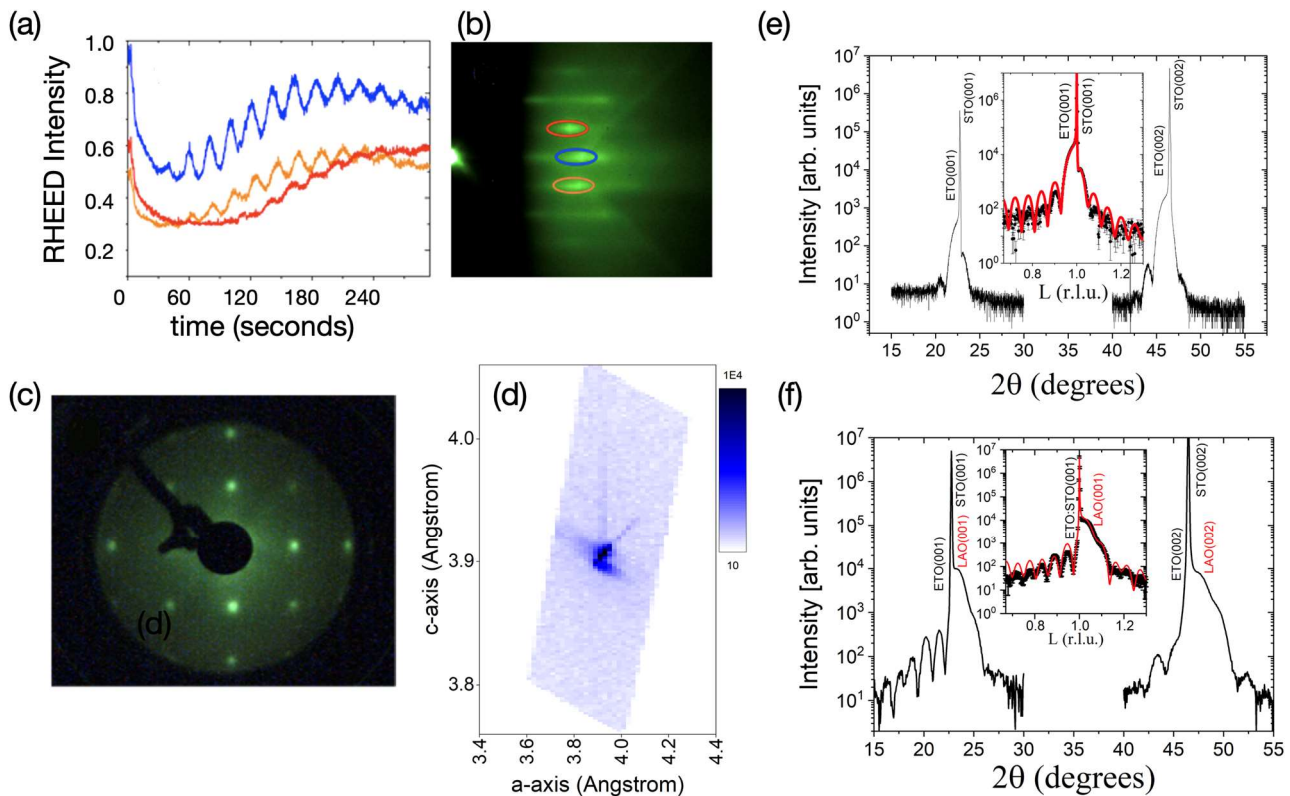* roberto.dicapua@unina.it
** marco.salluzzo@spin.cnr.it

Fig. S1: a) Real-time intensity oscillation of the specular (blue) and first order (1 0) and (-1 0) (orange and red curves) diffraction spots in the RHEED pattern during the growth of a 15uc ETO films. b) Corresponding RHEED pattern at the end of the deposition. The ellipses represent the regions used to integrate the intensity shown in a) with their corresponding color code. c) LEED pattern, on the same film, after the post-annealing process. (d) ex-situ x-ray diffraction reciprocal space x-ray diffraction map around the (103) reflection. (e) and (f) θ-2θ pattern on the 15 uc ETO/STO film measured by ARPES and of a LAO(11uc)/ETO(8uc)/STO heterostructure grown in the same conditions, respectively. Both data show Pendellösung fringes around the main diffraction peak. In the insets we show the (001) diffraction peaks and their fit (red lines).

S2 – Ferromagnetic characterization of EuTiO₃ (ETO) films

We performed Eu $M_{4,5}$ and Ti $L_{2,3}$ edges x-ray magnetic circular dichroism (XMCD) measurements in total electron yield (TEY) mode on representative samples protected (capped) or not-protected (uncapped) by a $LaAlO_3$ overlayer, namely $LaAlO_3/EuTiO_3/STO$ heterostructures and $EuTiO_3$ thin films. In particular, in Fig. S2, we show XMCD data at 6.5 and 0.1 Tesla on 8uc (3nm) $EuTiO_3$ films (Fig.S2a-c) and on a similar sample covered by a 4 nm LAO epitaxial film (Fig. S2d-f), grown in the same conditions of the samples measured by ARPES.

The comparison between capped and uncapped ETO shows a sizeable XMCD-signal at the Eu $M_{4,5}$ and Ti-$L_{2,3}$ edges in both cases. However, only the capped sample is characterized by XAS and XMCD spectra typical of Eu^{2+} oxidation state, with only a minor percentage of Eu^{3+}, and an Eu spin moment close to the value expected for Eu in Eu^{2+} valence state. It is also clear from the data that in the large part of the uncapped (and air exposed) ETO, Eu-ions change valence from Eu^{2+} to Eu^{3+} (Fig. S2a). As the probing depth in TEY at 1100 eV is of the order of 8-10 nm (and 2 nm at the 460 eV), the valence change happens at the surface and in a substantial fraction of the investigated sample (3 nm thick). These data show that in uncapped samples after exposure to air, Eu^{2+} valence changes to Eu^{3+} in a substantial fraction, which explains the reduced XMCD signal. Yet, the data show a clear Ti-$L_{2,3}$ edge XMCD even in uncapped ETO at 0.1 Tesla, although it was air-exposed, showing that ETO has a finite splitting of Ti-3d states.

We also performed SQUID magnetometry on the capped LAO/ETO sample and on the unprotected ETO/STO 15uc film measured by ARPES. As shown in suppl. Fig. S2g), a clear hysteresis in the magnetization at low temperature (3 and 4 K), disappearing at 10 K is observed. In protected ETO, as expected, a total saturated magnetic moment of about 6.8 m_B/Eu, close to the one expected from Eu^2, is found, while the unprotected ETO show a reduced saturation magnetization of about 4.0 m_B/Eu due to the presence of non-magnetic Eu^{3+}. These results demonstrate unambiguously that $EuTiO_3$ films are ferromagnetic, with a T_c below 10 K.
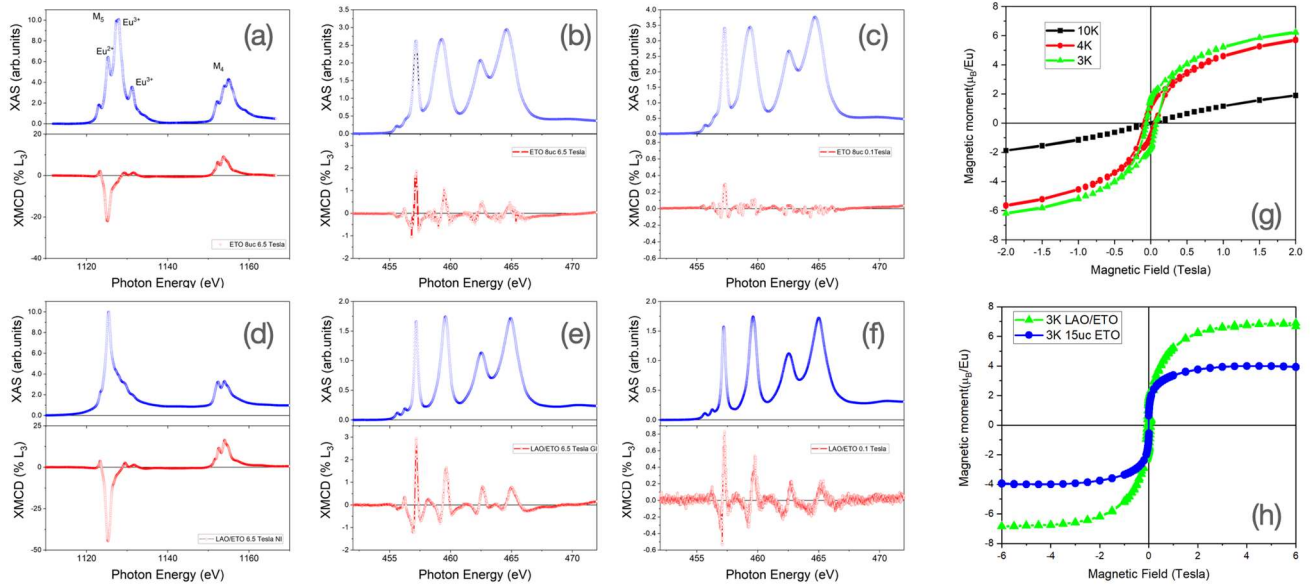
Fig. S2: Eu-M$_{4,5}$ edge and Ti-L$_{2,3}$ edge XAS and XMCD data on uncapped (a)-(c) and LAO-capped (d)-(f) ETO films. (a)-(b) and (d)-(e) spectra are measured at 6.5 Tesla, while (c) and (f) Ti-L$_{2,3}$ edge XAS and XMCD data are measured at 0.1 Tesla. The data are acquired in grazing incidence (70 degrees from the surface normal) in total electron yield mode at 3K.(g) SQUID magnetometry on LAO capped 8uc ETO/STO sample at three temperatures, 3K, 4K, and 10K, and (h) comparison on large field range with SQUID magnetometry data on 15uc ETO. The well-known diamagnetic contribution of the STO substrates has been subtracted from the data.

S3 Supplementary dispersion maps as function of the ETO thickness

We show in Fig. S3 the evolution of the band dispersions of ETO thin films as function of the thickness i.e., 2, 5 and 15 uc ETO deposited on insulating, TiO$_2$ terminated, STO single crystals and of 15uc ETO deposited on a buffer SrRuO$_3$ metallic layer.

From the thickness evolution, we notice that 2uc ETO shows a band dispersion quite different from thicker ETO films. In particular the band bottom is around -60 meV much higher than that one of thicker ETO, (-160 meV), and the splitting between heavy and light bands is very small (if any).

This result suggests that the in 2uc ETO the surface state is not fully developed and that we do see contributions from the STO bulk. At 15 uc, ARPES data of the sample deposited on bare insulating STO and on SRO buffer are quite similar, with similar Fermi momentum and band bottom. As expected, the signal to noise ratio is much higher in the sample deposited on conducting SRO.
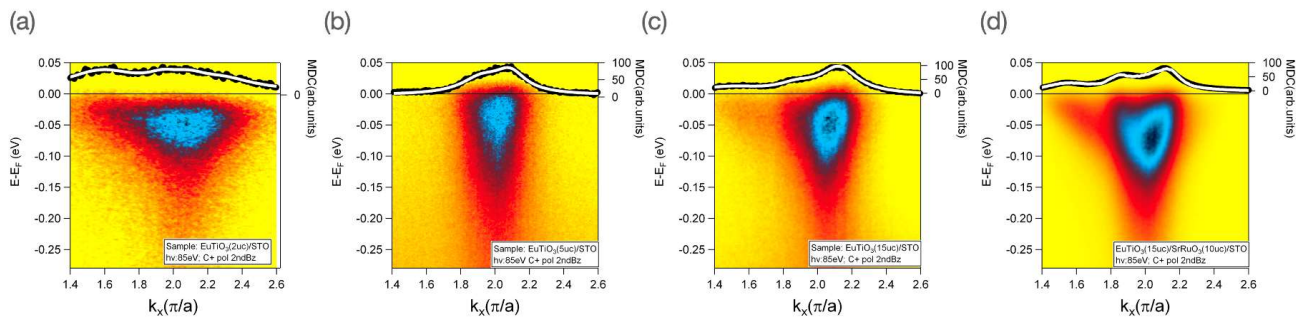

Fig. S3: Evolution of the band dispersion measured with hν = 85 eV and C+ polarization: (a) 2uc ETO on STO; (b) 5uc ETO on STO; (c) 15uc on STO; (d) 15 uc ETO on SRO buffer layer deposited on STO.

In Table S1 we compare the values of the Fermi momentum, the band bottom for heavy and light bands estimated from the analysis of MDC-curves at the Fermi level and at several energies below E$_F$, combined to analysis of the 2D-curvature maps of the data ([S2]).

Table S1: values of the Fermi momenta of the different bands identified in the band dispersion cuts. For the 5uc sample the value of k_F for heavy bands cannot be determined from the dispersion map, being too week. On the other hand, signatures of heavy bands are seen in the Fermi surface data shown in Fig.1 of the main text. E(0) is the band bottom.

Sample	k_F (Å^{-1}) $3d_{xy}$	k_F (Å^{-1}) $3d_{xz}$	k_F (Å^{-1}) $3d_{yz}$	$-E_0$ (meV) Light band	$-E_0$ (meV) Heavy bands
2uc ETO/STO	0.08±0.01	0.08±0.01	0.40±0.01	60±5	60±5
5uc ETO/STO	0.07±0.01	-	-	80±5	-
15uc ETO/STO	0.13±0.01	0.08±0.01	0.37±0.01	150±5	90±5
15ucETO/SRO/STO	0.135±0.005	0.090±0.005	0.35±0.01	160±5	100±5

S4-Overview of the valence band dispersion of ETO q2DEG

In Fig. S4, we show the valence band k_x- dispersion map (a), and its corresponding curvature map (b) (ref. [S2]) on a large binding energy range acquired with 85 eV incoming photons and C+ polarization around the Γ-point. One can see the almost non dispersing character of the Eu-4f band, in contrast with the more dispersing character of O-2p bands.
In Fig. S4c we show an energy dispersive curve average over -0.5 to 0.5 Å^{-1} momentum around the gamma point showing the quasiparticle peak and the long tail of the Eu^{2+} $4f^7$ peak at -2 eV.
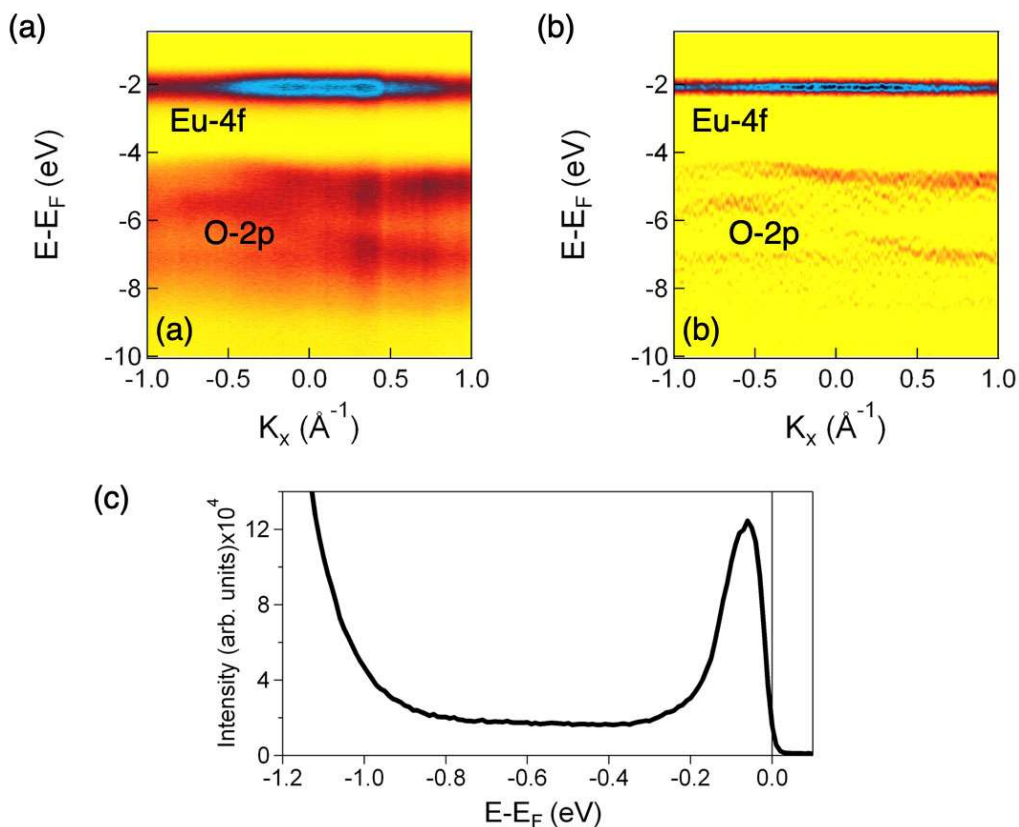

Fig. S4 a) Valence band dispersion of ETO q2DEG showing the Eu-4f and the O-2p bands and (b) corresponding curvature map. (c) Energy dispersion curve average over -0.5 to 0.5 Å^{-1} momentum around the gamma point, which show the quasiparticle peak merging with the long tail of the -2eV Eu4f band.

S5 - MDC analysis.

Momentum Dispersion Curves (MDCs) allow to localize maxima of ARPES signal in the E-k_x dispersion maps, for the identification and the attribution of the recorded band features. In Fig. S5 we report examples of MDC profiles analysis on a 15uc ETO/SRO/STO sample, at different binding energy values E (referred to the Fermi level E_F as $E - E_F$). The MDC profile corresponding to a given E value is obtained by averaging ARPES intensity values at each k_x over an energy window of 10 meV (centered on the chosen E). The analysis of each profile was performed through a deconvolution in terms of overlapping Lorentzian or Gaussian peaks (both of them providing similar fittings). In the reported maps, the light d_{xy} and the heavy one along the largest k_F value, d_{yz} emerge from the map recorded in s-polarization of incoming photons, while the d_{xz} band (heavy band along the direction of minimum k_F) can be observed in the p-polarization. At each given E value, the central k_x of each Lorentzian/Gaussian contribution defines the (k_x, E) point to be employed in the tight binding fitting procedure described in the following.
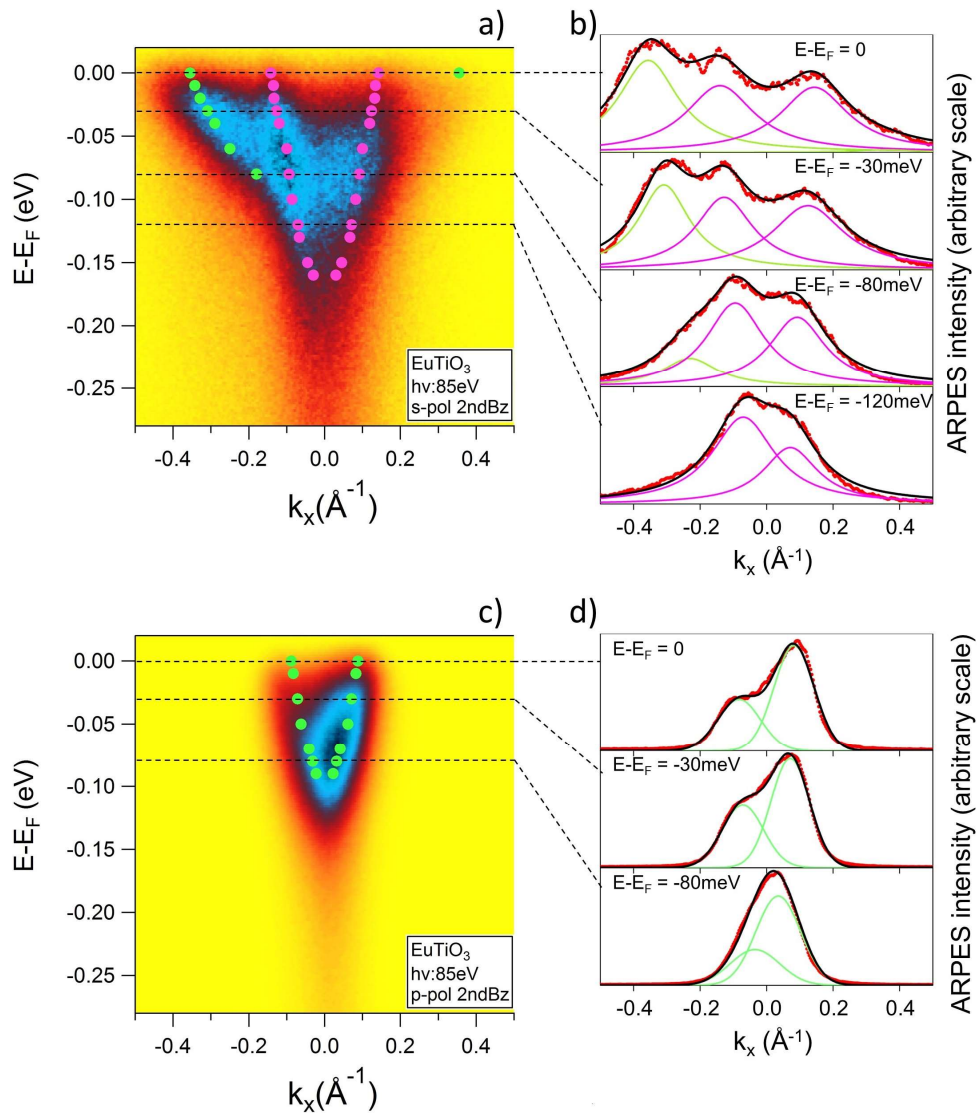

Fig. S5: High statistics band dispersion k_x-cuts (acquired around the Γ point in the second Brillouin zone, s- and p-polarization, cfr. main text) on the surfaces of the 15 uc ETO/SRO/STO film: example of MDC analysis for the extraction of (k_x, E) point to be employed in the tight binding fitting procedure described in the following. a) s-pol map, on which the points for the fitting are highlighted ($3d_{yz}$ as green circles, $3d_{xy}$ as magenta circles). b) MDC profiles for some of the binding energy values, with the peak deconvolution which leads to the identification of the points highlighted in panel a (contributions from the different bands are in the same color code as in panel a; the global fitting curve is reported as black line, the experimental data as red circles). c) p-pol map, on which the points for the fitting are highlighted ($3d_{xz}$ as green circles). d) MDC profiles for some of the binding energy values, with the peak deconvolution which leads to the identification of the points highlighted in panel c (the global fitting curve is reported as black line, the experimental data as red circles). For all the polarizations on all the investigated sample, we applied this procedure to infer the experimental points for the tight binding band fitting.

S6- Tight binding band fitting

In Fig. S6, we show the high statistics band dispersion k_x-cuts (around the Γ point in the Second Brillouin zone, cfr Fig. 2 main text) on 15uc ETO film, STO-A and STO-B samples, and the corresponding Fermi surfaces (k_x-k_y cuts).
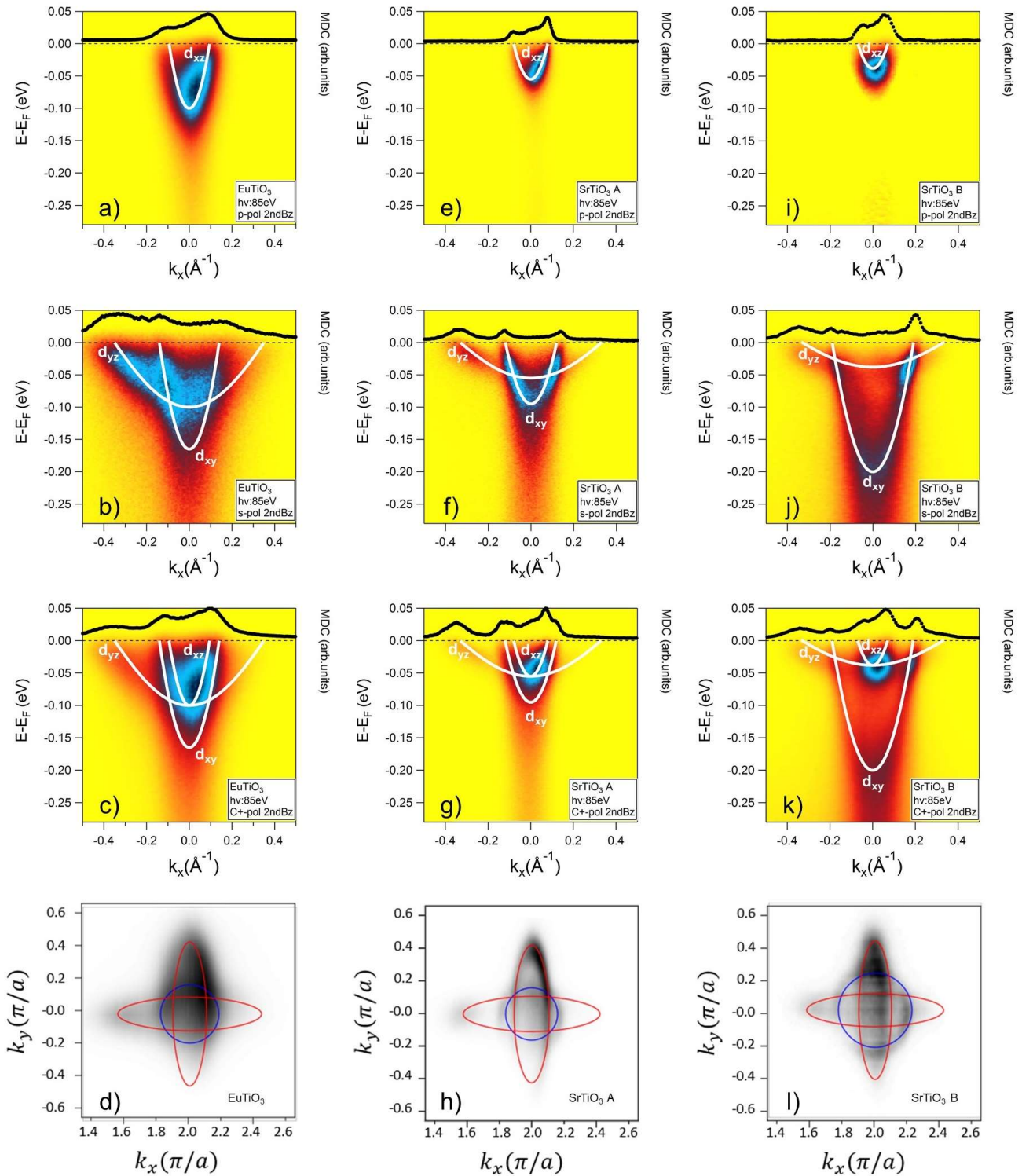

Fig. S6: High statistics band dispersion k_x-cuts and the relative k_x-k_y cuts of the Fermi surface (data acquired around the Γ point in the second Brillouin zone), together with the corresponding tight binding fits. The panels report: band dispersions for the 15 uc ETO film in p-polarization (a), s-polarization (b), C+-polarization (c), and the Fermi surface of the 15 uc ETO film (d); band dispersions for the STO-A sample in p-polarization (e), s-polarization (f), C+-polarization (g), and the Fermi surface of the STO-A sample (h); band dispersions for the STO-B sample in p-polarization (i), s-polarization (j), C+-polarization (k), and the Fermi surface of the STO-B sample (l). (in the Fermi surface plots, the blue circumference is the cut of the d_{xy} sheet, the red ellipses are the cuts of the d_{xz}-d_{yz} sheets)

Here we show p-, s-, and C+-polarization maps, in false color scale, and the tight binding fit for the band identification. The performed tight binding fits were then used to estimate the Fermi momentum and the effective masses of electrons in each band of the three samples. (see Table 1 in the main text). Circular polarization (C+) *E vs. k_x* band dispersions include features associated to all the bands in the system, namely bands with $3d_{xz}$, $3d_{yz}$ and $3d_{xy}$ characters; dataset recorded in *p-pol* configuration are mainly affected by the $3d_{xz}$ band, while *s-pol* configurations provide information about the $3d_{xy}$ and the $3d_{yz}$ bands. (d_{xy} indicates the light band, while d_{xz} and d_{yz} refer to the heavy band along the short and the long diameters of the ellipse, respectively). The band-dispersion profiles at the different polarizations were analyzed considering simple 2D tight binding dispersion relations [S3] taken at $k_y = 0$ as a function on only k_x. Assuming three independent bands, the fitting equations can be written in the following form:

$$E_{xy}(k_x) - E_F = V_{xy}(1 - \cos k_x a_0) + E_{0xy}$$

$$E_{xz}(k_x) - E_F = V_{xz}(1 - \cos k_x a_0) + E_{0x}$$

$$E_{xy}(k_x) - E_F = V_{yz}(1 - \cos k_x a_0) + E_{0yz}$$

Where E_F is the Fermi energy, a_0 is the lattice constant of the cubic cell, V_{xy}, V_{xz}, V_{yz} are related to the so-called inner potentials, and E_{0xy}, E_{0xz}, E_{0yz}, being the $E - E_F$ value at $k_x = 0$, represent the band bottom (E_{0xz} and E_{0yz} are expected to have the same value inside the experimental error).

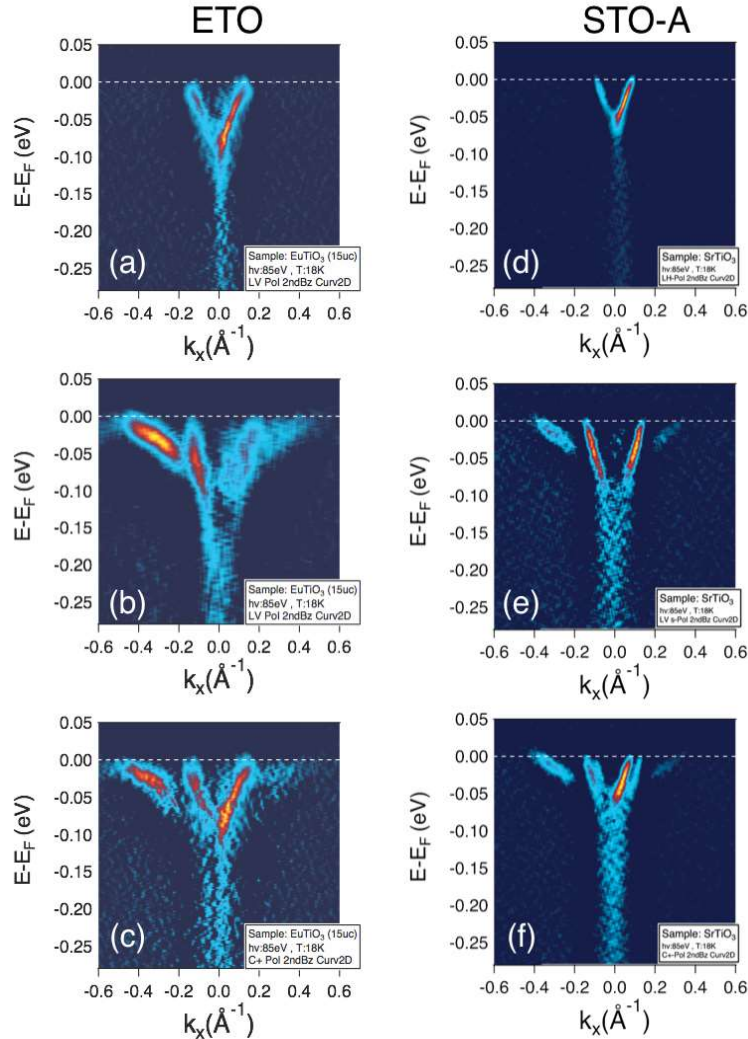## S7- Curvature maps

.

Fig. S7: High statistics 2D-curvature band dispersion maps for: a)-c) a 15 uc ETO film and d)-f) STO-A q2DEG. Panels a) and d) are for LH (p-pol) polarization, b)-e) for LV (s-pol polarization) and c) and f) for C+ polarization.

We applied the method described in ref. [S2] to extract 2D-curvature maps of the ARPES dispersions shown in Fig. 2 of the main text a to highlight the differences between ETO and STO electronic structure.

The curvature maps in Fig. S7 reveal that for both STO and ETO surface states the dispersion maps substantially deviate from independent bands modeled within a tight-binding scenario near the anti-crossing point and near the Fermi level, as confirmed by DFT+U calculations. In the ETO case, the deviation is more pronounced compared to the STO cases.

S8- Surface termination of EuTiO₃ films: XPS core level spectroscopy of Eu and Ti states, and DFT+U calculations on EuO terminated surface.

The main DFT+U calculations presented throughout the manuscript consider $EuTiO_3$ surfaces terminated with TiO_2. Here we provide experimental evidence and further DFT+U calculations, which suggests that the assumption is correct, i.e. our $EuTiO_3$ are TiO_2 terminated. First, we show in Fig. S8a,b core level spectroscopy data of the 15 uc ETO/SRO sample on which most of the analysis was focused on. In order to have info about the surface terminations, we used 600 eV energy photons to measure at the same time Ti-*2p* and Eu-*4d* core level spectra.

Eu-*4d* core level spectral features shown in Fig.S8a are typical of Eu in Eu^{2+} oxidation state. On the other hand, Ti-*2p* core level spectra are characterized by main Ti-*$2p_{1/2}$* and *$2p_{3/2}$* (Ti^{4+}) peaks, and shoulders at lower binding energy, associated to the presence of *$3d^l$*-Ti^{3+} states., which is due to the presence of Ti ions with a Ti^{3+} valence, a typical fingerprint of 2DEGs in titanates. Very strikingly, as shown in Fig. S8b, the intensity of the high energy satellite does not change going from normal (more bulk sensitive) to shallow emission (more surface sensitive), while the Ti^{4+} features strongly decrease. This indicates that Ti^{3+} valence states are at the surface. While these data are consistent with a TiO_2 termination, experimentally distinguishing the atomic surface termination needs further structural surface studies, like Grazing Incidence x-ray diffraction (GIXD), which should be done in future studies. It should be noted that the exact surface termination is also still an open question for the STO 2DEG [S4, S5].

In order to further support a TiO_2 termination of our ETO films, we show below band dispersion calculations for EuO terminated ETO. The calculations have been performed using exactly the same model and oxygen divacancy configuration described in the main text for TiO_2 terminated ETO (see inset of Fig. S8c).
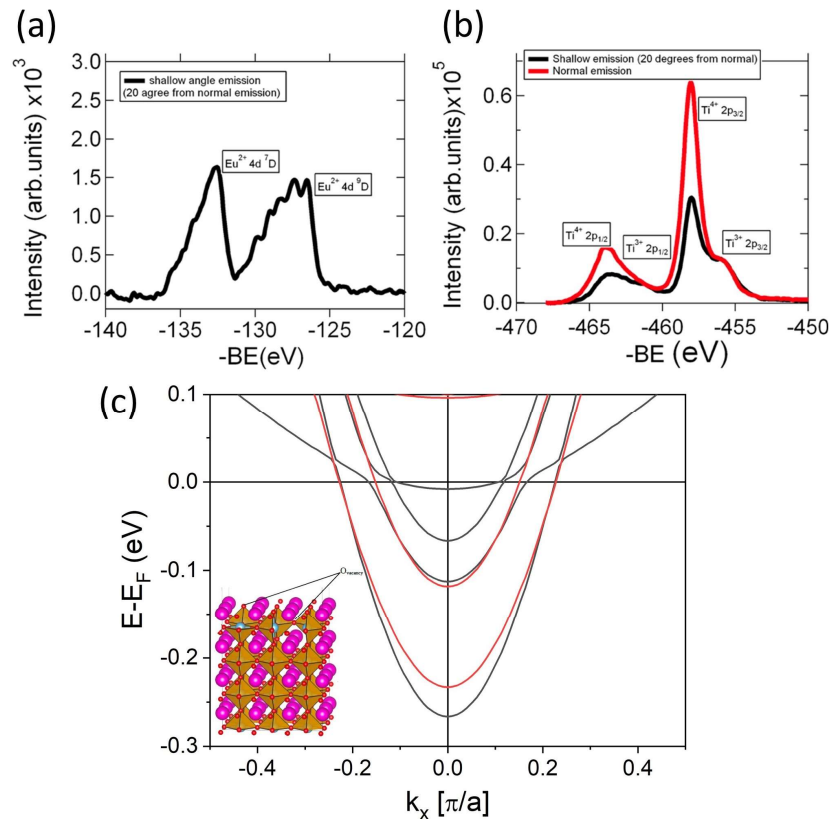

Fig. S8: Core level spectroscopy data of 15uc ETO deposited on buffer SrRuO₃: comparison between (a) Ti2p and (b) Eu4d core level spectra acquired in shallow emission angle (20 degrees from the surface normal) using incident photons at $h\nu$ = 600 eV. (c) Comparison between normal (red line) and shallow emission (black line) Ti2p core level spectra. (c) Calculated band dispersions around the Γ-point along Γ-X in EuO terminated 2x3x4 ETO (001) slab using PBESOL+U with same parameters employed for the TiO₂ termination and same oxygen divacancy.

One can see that also in the case the EuO termination the bands are spin-split, but the band bottom of the lowest lying band is of the order of 0.25 eV, about 1.5 times the one found experimentally. Moreover, heavy bands are above the Fermi level. Both results are in substantial disagreement with the experimental results, further confirming that the assumption of TiO_2 termination of our ETO films is possibly correct.

S9- Spin-Orbit Coupling (SOC) in the in-plane di-vacancy configuration

In Fig. S9 we report calculated band dispersions, with the SOC contribution, for ETO(001) and STO(001), considering configuration with an in-plane di-vacancy in a $2ax3ax4a$ supercell, described in the main text, with one missing oxygen in the topmost TiO_2 layer and a second one in the subsurface SrO/EuO layer at a distance of 6.2 Å of the STO(001) and ETO(001) surfaces, respectively (see Fig. 3a and 3b in the main text). See main text, Fig. 4a and 4b, for the analogous calculated band dispersions without SOC.
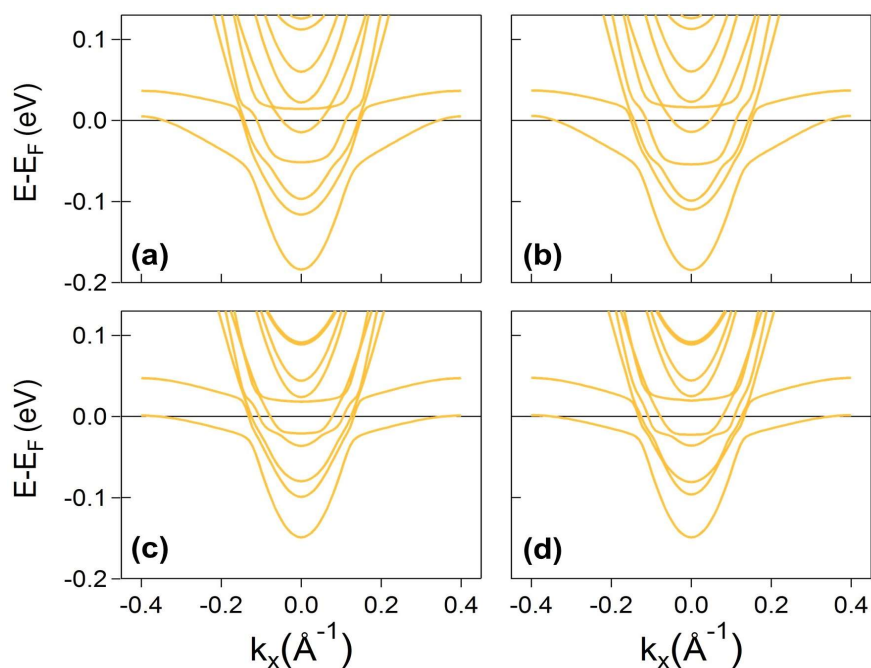

Fig. S9: Calculated band dispersions, including SOC, around the Γ-point along Γ-X in ETO (001) (upper panels) and STO (001) (bottom panels). a) and c) show calculations including SOC with magnetization direction along [001], while b) and d) show calculations including SOC with magnetization direction along [100]

S10- Vertical di-vacancy configuration

Among the different structural configurations, alternative to the one reported in the main text, on which we performed DFT+U calculation, we report here (Fig. S10) the results obtained considering a vertical divacancy in a $2ax2ax7a$ supercell, with missing oxygens in the first and second subsurface SrO/EuO layers of the STO(001) and ETO(001) surfaces, respectively.

Spin density integrated between -0.15 eV and the Fermi level, and layer- and element-resolved density of states, are also shown for both compounds. The calculated band dispersions (see comments in the main text) around the Γ-point along Γ-X and Γ-M directions are reported in the lower panels (Figs. S10g-l).
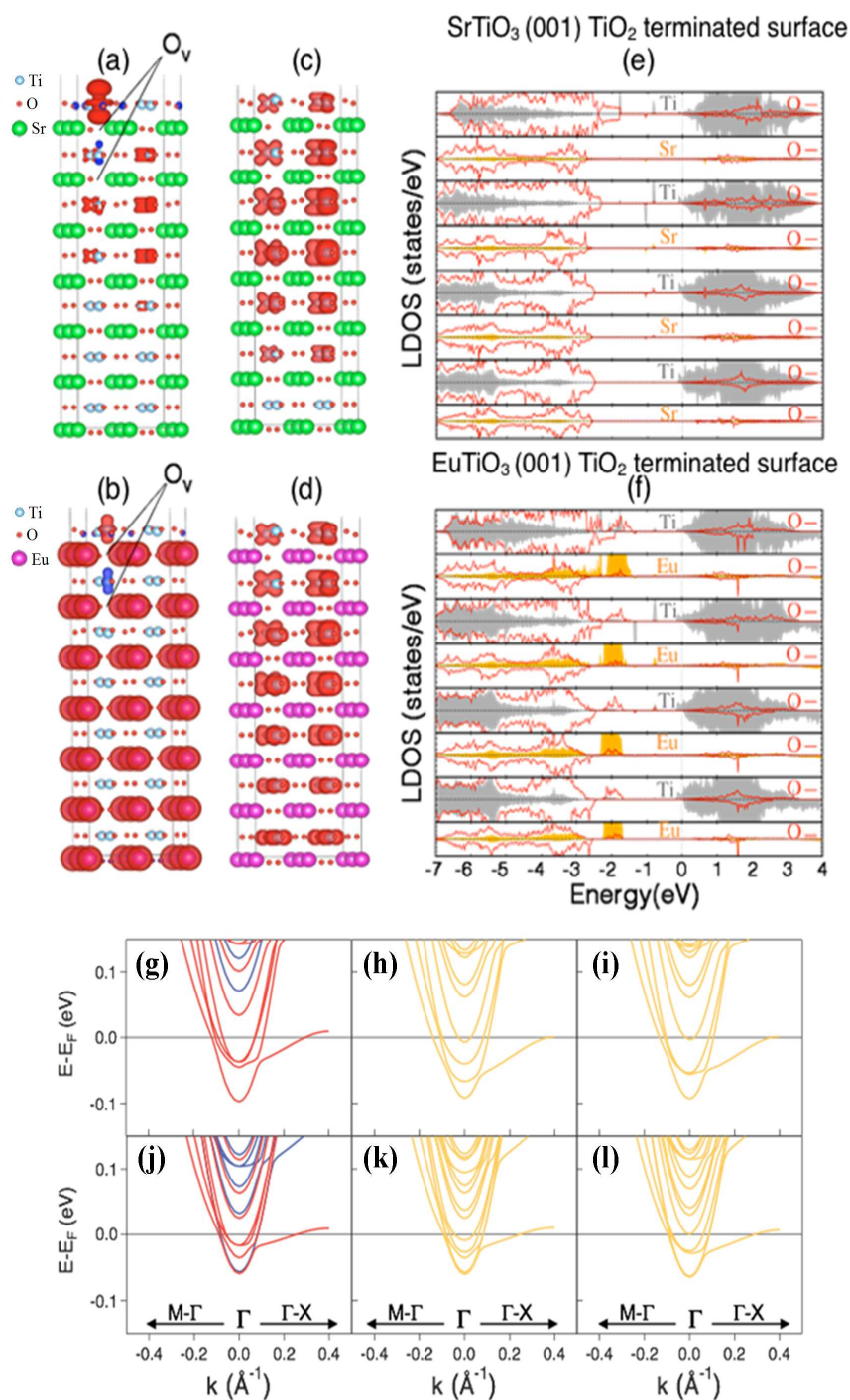
Fig. S10: side views of the relaxed (a) STO(001) and (b) ETO(001) surfaces with vertical oxygen divacancy in the first and second subsurface SrO/EuO layers. The panels show also the spin density with iso-values of 0.0005 e/Å³ for the two systems. Red/blue corresponds to majority/minority spin density. (c)-(d) Spin density, integrated between -0.15 eV and the Fermi level of STO(001) (c) and ETO(001) (d). (e) and (f) Layer- and element-resolved density of states showing the spatial distribution and orbital polarization of the q2DEG in STO (001) and ETO(001), respectively. Calculated band dispersions around the Γ-point along Γ-X and Γ-M directions in ETO(001) (panels g,h,i) and STO(001) (panels j,k,l). (g) and (j) show the results without spin-orbit coupling (SOC) (red/blue correspond to majority/minority bands), h) and k) show calculations including SOC with magnetization direction along [001], while and l) show calculations including SOC with magnetization direction along [100].

S11- Comparison between the DFT-U planar di-vacancy configuration model and experimental data

In Fig. S11 we show a comparison between the ETO and STO (sample: STO-A) ARPES band dispersion data and DFT+U calculations (ground state) obtained considering configuration with an in-plane di-vacancy in a $2ax3ax4a$ supercell, considered in the main text, with one missing oxygen in the topmost TiO_2 layer and a second one in the subsurface SrO/EuO layer at a distance of 6.2 Å of the STO(001) and ETO(001) surfaces, respectively (see Fig. 4a and 4b in the main text).
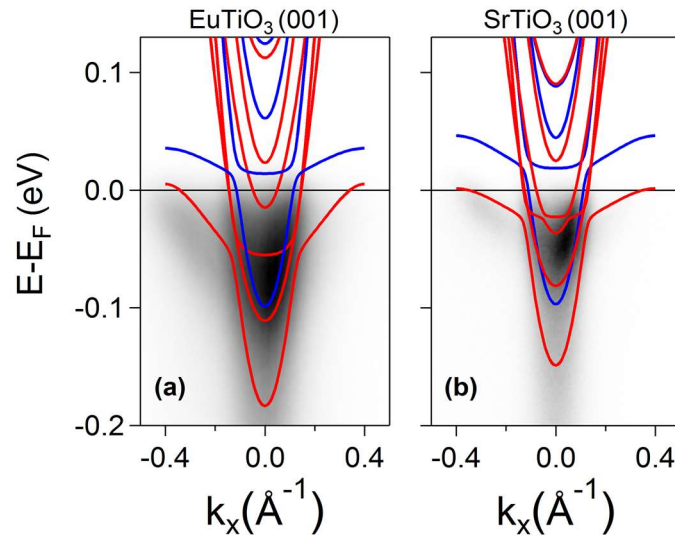

Fig. S11: Comparison between C+ ARPES data acquired at hv=85eV and DFT+U calculations with the model described in the main text, around Γ-point along Γ-X direction, for (a) ETO(001) and (b) STO(001) (sample STO-A).

S12- Comparison between structural distortion at the STO and ETO surface in the DFT+U planar di-vacancy configuration model

In order to compare the structural distortion in STO(001) and ETO (001), we list the Ti(X)-O-T(Y) in-plane (Table S2) and out-of-plane (Table S3) bond angles. Labels X and Y indicate different Ti-ions in the adopted structural configuration, as illustrated in Fig. S12.
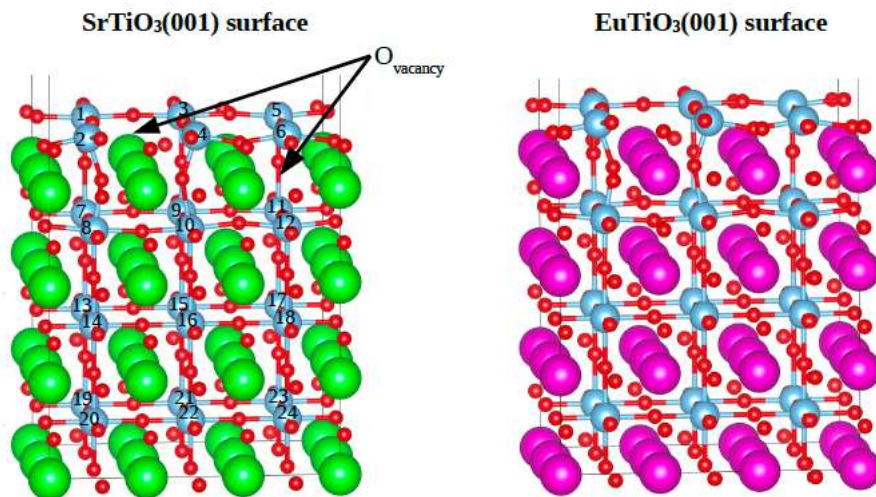

Fig. S12: supercells of STO (001) (on the left) and for ETO (001) (on the right), showing the labelling used to identify different Ti-ions (for ETO the same labeling shown for STO has been used).

Table S2: In-plane Ti(X)-O-Ti(Y) bonding angles for STO (left column) and ETO (right column). All angles not listed have the ideal value of 180°.

	SrTiO₃(001) surface	EuTiO₃(001) surface
In-plane	Angle (°)	Angle (°)
Ti1-O-Ti2	161.8	161.6
Ti1-O-Ti3	176.0	177.0
Ti3-O-Ti4	162.0	162.0
Ti3-O-Ti5	173.4	173.0
Ti5-O-Ti6	179.3	179.3
Ti4-O-Ti6	161.8	161.5
Ti7-O-Ti8	175.8	175.7
Ti7-O-Ti9	175.6	174.9
Ti9-O-Ti10	175.8	175.7
Ti9-O-Ti11	177.5	177.8
Ti11-O-Ti12	173.0	173.0
Ti10-O-Ti12	168.0	168.0

Table S3: Cross-plane Ti(X)-O-Ti(Y) bonding angles for STO (left column) and ETO (right column). All angles not listed have the ideal value of 180°.

	SrTiO₃(001) surface	EuTiO₃(001) surface
Cross-plane	Angle (°)	Angle (°)
Ti1-O-Ti7	179.1	178.1
Ti2-O-Ti8	154.0	152.3
Ti3-O-Ti9	179.1	178.1
Ti4-O-Ti10	154.0	152.3
Ti5-O-Ti11	180.0	180.0
Ti7-O-Ti13	180.0	180.0
Ti8-O-Ti14	179.3	179.2
Ti9-O-Ti15	180.0	180.0
Ti10-O-Ti16	179.3	179.2
Ti11-O-Ti17	180.0	180.0
Ti12-O-Ti18	180.0	180.0

We can notice that the oxygen defects on the surface reduce the symmetry. Hence, distortions take place mostly around the oxygen vacancies, i.e. at the surface. In-plane distortions (Table S2) are very similar in both ETO and STO, while there are more pronounced, although quite limited, differences along the cross-plane (c-axis) (Table S3).
Distortions occur only in the top two layers from the vacuum, leaving surfaces beneath close to be undistorted.

Supplementary References

[S1] M. Björck and G. Andersson . *Appl. Cryst.* **40**, 1174-1178(2007).
[S2] P. Zhang, P. Richard, T. Qian, Y. M. Xu, X. Dai, and H. Ding, *Rev. Sci. Instrum.* **82**, 043712 (2011).
[S3] Z.S. Popovic, S. Satpathy, and R.M. Martin, *Phys. Rev. Lett.* **101**, 256801 (2008).
[S4] A. Fragneto, G. M. De Luca, R. Di Capua, U. Scotti di Uccio, M. Salluzzo, X. Torrelles, T.-L. Lee, and J. Zegenhagen, *Appl. Phys. Lett.* **91**, 101910 (2007).
[S5] S. N. Rebec, T. Jia, H. M. Sohail, M. Hashimoto, D. Lu, Z.-X. Shen, and R. G. Moore, *PNAS* **116**, 34 16687 (2019).